applied sciences

MDPI

Article

Fatigue, Fracture, and Damage Tolerance of Ultrahigh-Strength Martensitic Tendon-Rods for Structural Engineering

Patricia Santos [1,2], Mihaela Iordachescu [1,*], Andrés Valiente [1] and Elena Scutelnicu [3]

[1] Material Science Department, ETSI Caminos, Polytechnic University of Madrid, 5 Prof. Aranguren St., 28040 Madrid, Spain; patricia.santos@upm.es (P.S.); andres.valiente@upm.es (A.V.)
[2] Applied Physics and Materials Engineering Department, ETSI Industriales, Polytechnic University of Madrid, 2 José Gutiérrez Abascal St., 28006 Madrid, Spain
[3] Manufacturing Engineering Department, Faculty of Engineering, "Dunarea de Jos" University of Galati, 80008 Galati, Romania; elena.scutelnicu@ugal.ro
* Correspondence: mihaela.iordachescu@upm.es

Abstract: The paper addresses the fatigue resistance, fracture behavior, and damage tolerance of a new type of ultrahigh-strength bar for prestressing concrete made of a low-alloy lath martensitic steel. The fracture tests show that the bar steel has a medium-high fracture toughness of 75 MPa $m^{1/2}$ and a fatigue cracking resistance that fits the Paris-Erdogan Law as most of Eurocode 3 structural steels. The damage tolerance analysis combines two failure assessment diagrams (FADs), the first focused on the damage level and the second on toughness and yielding capacity as material properties of the bar steel, whose influence and interaction are determinant for failure. The location of the experimental failure data in the FADs indicates that the steel is endowed with a combination of strength, ductility, and toughness able to prevent unexpected failures. The damage micro-mechanisms revealed from the examination of broken specimens differ from fatigue to fracture cracking, but in a manner consistent with the observed mechanical behavior and microstructure of the bar steel.

Keywords: lath martensitic steel; fracture toughness; fatigue resistance; damage tolerance

Citation: Santos, P.; Iordachescu, M.; Valiente, A.; Scutelnicu, E. Fatigue, Fracture, and Damage Tolerance of Ultrahigh-Strength Martensitic Tendon-Rods for Structural Engineering. *Appl. Sci.* **2024**, *14*, 11543. https://doi.org/10.3390/app142411543

Academic Editors: Xiaoyong Wang and Ki-Bong Park

Received: 17 November 2024
Revised: 3 December 2024
Accepted: 9 December 2024
Published: 11 December 2024

1. Introduction

The accurate geometrical configuration and reliable loading control provided by the high-strength steel bars for pre- or post-stressed concrete make them a versatile tool for applying the sustainability and resilience criteria incorporated in the modern technical codes [1,2], especially those affecting construction and rehabilitation of critical structures for public safety, such as tunnels, gas storage tanks, but above all bridges, both in prestressed and cable-stayed variants [3–7]. However, the minimum tensile strength required for these steel bars is 1 GPa [7,8], which severely limits the types of bars available to this end. In the case of the bars with pearlitic microstructure, such a high tensile strength is acquired by applying adequate heat treatments to hot-rolled rods during manufacturing. Despite this, the bars exhibit moderate ductility, low toughness, and limited resistance to stress corrosion cracking under constant or fluctuating carrying loads [4].

In the last two decades, new types of martensitic steel bars that meet the tensile strength requirement have been developed with the aim of improving toughness and enhancing the ductile to brittle transition temperature [9–12]. Their improved properties are a consequence of the hierarchical microstructure of the steel, which results from dividing the prior austenite grains into several structural units with different length scales, i.e., lath, sub-block, block, and packet [6]. In addition, the steel may contain small angular patches of retained austenite and discrete inclusions related to microalloying [13,14]. It is generally accepted that the addition of Cr, Ni, Ti, V, and Mo significantly improves the mechanical properties of lath martensite steel bars, even though there is a degree of controversy regarding the detrimental effect of their hierarchical microstructure on fatigue crack propagation [15,16]. In response

to such a major concern in relation to the structural use of these bars, a considerable research effort has been dedicated to the assessment of the fatigue cracking resistance, especially in the second stage of fatigue, i.e., once the cracking process is initiated [17,18]. The results showed that the crack propagation direction may change when the crack encounters hard phase particles or boundaries of martensitic blocks with different orientations, though it can be arrested at martensitic packet boundaries [17,19–22].

The object of this research is a new variant of a lath martensitic, ultrahigh steel bar recently manufactured for prestressing concrete structures. In this view, the paper addresses aspects of the steel behavior critical for the potential use of these bars as components of structural tendons, related to resilience and durability. According to this purpose, the fatigue and fracture resistance of this new lath martensitic steel are explored and discussed, the findings being considered new and useful information for the structural engineering and construction industry. Moreover, new insights related to damage tolerance are analyzed on the basis of two failure diagrams that consider the influence and interaction between the damage level, fracture resistance, and yielding capacity of the steel bars.

2. Material and Testing Methods

2.1. Material Characteristics

The tested ultrahigh-strength lath martensitic steel belongs to 23 mm diameter bars, manufactured by hot-rolling and subsequent tempering, and is being recommended as a new steel product for prestressing of concrete. Table 1 gives the average of the elemental composition of steel determined on 3 tested samples with a carbon/sulfur analyzer (G4 ICARUS, Bruker AXS GmbH, Karlsruhe, Germany) and an Inductively Coupled Plasma Optical Emission Spectrometer (Thermo Fisher Scientific Inc., Waltham, MA, USA). Table 2 provides the mechanical characteristics of the steel obtained by tensile testing 5 mm diameter cylindrical specimens, machine-cut parallel to the bar axis. The tests were performed at a 1 mm/min constant crosshead speed by using a 200 kN servo-hydraulic machine (Instron 8501, Instron, Norwood, MA, USA), equipped with a load cell of 50/25 kN static/dynamic. As illustrated in Figure 1a, a conventional, resistive extensometer of 12.5 gauge length was employed for the elongation measurement and further strain computing. Figure 1b shows the moderately ductile fracture of one of the 5 tested specimens. The acquired load-elongation data were collected, processed, and further used for the characterization of the bar steel in accordance with the ISO 15630-3 [23].

Table 1. Chemical composition of the studied steel bars.

C *	Mn	Si	P	S *	Cu	Ni	Cr	Mo	Ti	V	Fe
0.45 ± 0.01	0.65 ± 0.04	1.77 ± 0.10	0.017 ± 0.004	0.004 ± 0.002	0.01 ± 0.01	0.06 ± 0.01	0.15 ± 0.04	0.02 ± 0.01	0.03 ± 0.01	0.003 ± 0.001	Bal

* determined with the C/S analyzer.

Table 2. Mechanical properties of the studied steel bars.

Elastic Modulus, [GPa]	Yield Strength, [MPa]	Tensile Strength [MPa]	[%] of Maximum Uniform Elongation
220	988	1138	8

The image illustrated in Figure 1c, acquired with a scanning electron microscope, SEM (XB 540, Carl Zeiss Microscopy GmbH, Jena, Germany), equipped with a focused ion beam (FIB), shows that the main microstructure of the bars is lath martensite, successively grouped in randomly arranged blocks and packets formed by dividing the prior austenite grains. In addition, the presence of some disperse inclusions is marked in Figure 1c with white arrows. The higher magnification detail captured in Figure 1d reveals two grouped, globular inclusions, the first of about 1.5 μm in diameter and the second smaller than 1 μm, which together might influence the fracture of the bar steel.

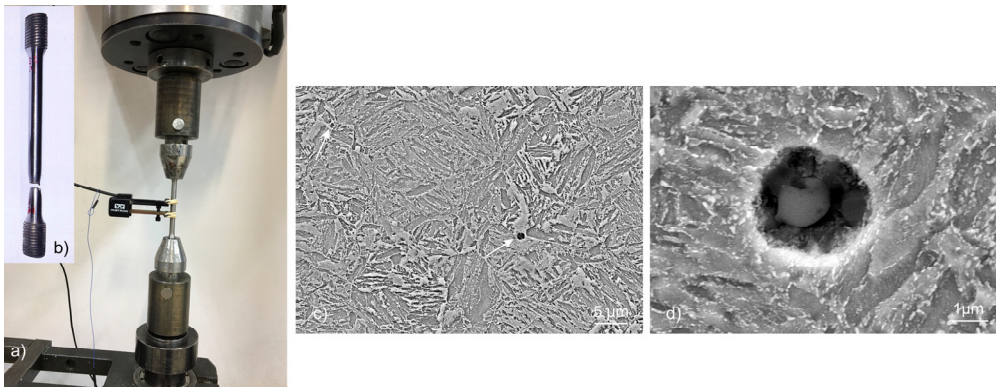

Figure 1. Images showing the: (**a**) tensile testing of smooth cylindrical specimens; (**b**) the moderately ductile fracture in tension of the steel; (**c**) representative microstructure of steel (the white arrows are indicating some inclusions); (**d**) higher magnification detail illustrating two grouped, globular inclusions.

2.2. Fracture Toughness and Fatigue Resistance Testing Procedures

The fracture toughness of the steel was determined on the basis of the ASTM E1304 [24] procedure, which involves the use of a short-bar specimen (SBS) with a geometrical configuration compatible with the dimensions of the studied bars, presented in Figure 2a. Since ASTM E1304 [24] requires a minimum of three tests to be performed, three SBS specimens were prepared for fracture toughness testing. In order to assure the fracture test's validity, conditioned by the crack growth in the small-scale yielding regime, the chevron notches of the tested SBSs were fatigue precracked. This involved the use of the same servo hydraulic equipment as for the tensile tests, with the load cell operating in dynamic mode. An average of 12,000 loading cycles in the load range of 0.5 to 3 kN, at a frequency of 8 Hz, were applied to each of the three specimens (SBS_1, SBS_2, and SBS_3), of thickness B = 12 mm and length W = 17.4 mm. A crack mouth opening displacement (CMOD) resistive extensometer was employed to control their cracking progress during fatigue, which was interrupted after reaching distinct crack extensions, as follows: 9.45 mm for SBS_1, 10.22 mm for SBS_2, and 11.14 mm for SBS_3. In the subsequent fracture tests, illustrated in Figure 2b, the same CMOD extensometer was used to monitor the failure process. Figure 2c shows the macroscopic image of one of the tested specimens, revealing the fatigue crack and its final fracture.

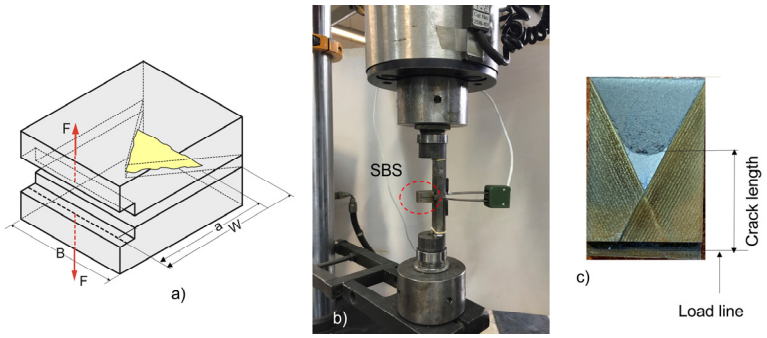

Figure 2. (**a**) Geometry and test configuration of SBS specimens (B = 12 mm, W = 17.4 mm); (**b**) image showing the fracture toughness testing of SBS specimens; (**c**) macroscopic image of one of the fracture surfaces of specimens with the marked crack length, a, measured according to ASTM E1304 [24].

The fatigue behavior of the bar material was assessed by means of cyclic tensile tests made with 5 mm diameter cylindrical specimens, in accordance with the sketch given in Figure 3a. Each specimen was surface notched (Figure 3b) to a depth of 0.5 mm before being subjected to several cyclic loading steps at room temperature at a frequency of 8 Hz.

During each step, the load amplitude was maintained constant and decreased between each two successive steps by 20% to assure that the applied load is constantly well below the yield strength of the specimen in the corresponding cracked condition. In order to maximize the number of experimental data, after each cyclic loading step, the specimens were unloaded and the cracked areas were progressively marked by heat tinting, as it is shown in Figure 3c. In addition, the crack size was determined from the specimen stiffness obtained after each fatigue step by measuring the load-CMOD curve slope during the static unloading process. The CMOD measurements were made by using a resistive extensometer, mounted on the surface of the specimen, just ahead of the notch, on a 12.5 mm length. At the end of each fatigue test, the specimens were broken in tension. The failure loads, together with the final crack dimensions, were further used to find out the critical stress intensity factor K_c for its further comparison with the determined fracture toughness measured from the SBS tests.

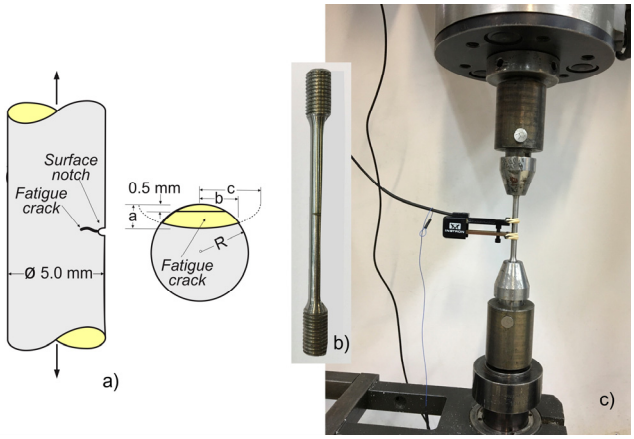

Figure 3. (**a**) Notched cylindrical specimen; (a, c—semi-axes of the ellipse assimilated to the fatigue crack front, b—half-width of the fatigue crack, and R—specimen radius); (**b**) image of the notched specimen; (**c**) image captured during the fatigue tests.

Lastly, the fracture morphologies in the fatigue crack propagation regime and in the final stage of fracture, further examined by SEM (equipped with an energy-dispersive X-ray analyzer—EDS, Oxford Instruments, Abingdon, Oxfordshire, UK), complement the macroscopic evaluation of the fracture behavior of the bar steel.

3. Results and Discussion

3.1. Fracture Toughness and Critical Stress Intensity Factor

Figure 4 shows the plots of the applied tensile load vs. CMOD obtained from the fracture tests of the three tested SBS specimens. The linearity of the obtained load-CMOD curves remains up to failure, which indicates that this takes place in a small-scale yielding regime and entails that the measured toughness is size independent. The slopes of the linear parts of the three curves are consistent with the respective crack sizes, which are 9.45 mm in SBS_1, 10.22 mm in SBS_2, and 11.14 mm in SBS_3. The first graph (Figure 4a) corresponding to SBS_1 indicates that the crack front remains stationary until the critical load is reached and the specimen suddenly collapses. In the other two cases (Figure 4b,c), the collapse is preceded by a number of pop-ins under decreasingly lower loads, so that the first of them was identified as being the fracture load P_m (Table 3). The pop-in occurrence can be explained by the decrease that experiences the stress intensity factor for this specimen configuration when the crack grows. Nevertheless, the pop-ins are likely to be activated by microstructural singularities that fail locally and cause the crack jumping. The probability of this crack behavior increases with the high presence of singularities.

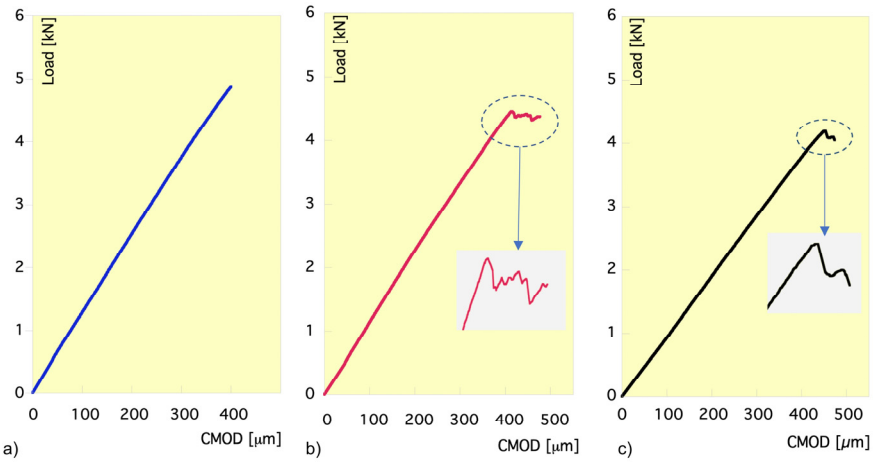

Figure 4. Load-CMOD plots in the fracture toughness tests of specimens: (**a**) SBS_1; (**b**) SBS_2; (**c**) SBS_3.

Table 3. Fracture tests data and results obtained with the SBS specimens.

Tested Specimen	Crack Length, a [mm]	Load, P_m [kN]	a/W	Y(a/W)	K_{Ic} [MPa $m^{1/2}$]
SBS_1	9.45	4.87	0.54	25.38	78.23
SBS_2	10.22	4.46	0.59	25.92	73.03
SBS_3	11.14	4.20	0.64	27.36	72.59
					Average: 75 MPa $m^{1/2}$

According to ASTM E1304 [24], the yield stress σ_{ys} = 988 MPa of the tested steel and the selected thickness, B = 12 mm, of the SBS specimen meet the condition to obtain a valid fracture toughness K_{Ic}, because the measured toughness values were lower than the limit σ_{ys} $(0.8\ B)^{1/2}$ = 110 MPa $m^{1/2}$. The bar steel fracture toughness K_{Ic} was obtained by particularizing Equations (1) and (2) for the experimental values of the fracture load P_m and the fatigue crack depth a, the latter measured by optical microscopy on the fracture surfaces of specimens and expressed as a fraction of the length of the specimen, $\tilde{a} = a/W$ [25]:

$$K_{1c} = Y\left(\tilde{a}\right)\frac{P_m}{B\sqrt{W}} \quad (1)$$

$$Y\left(\tilde{a}\right) = \exp\left(12.2903 - 56.9\tilde{a} + 136.83\tilde{a}^2 - 151.34\tilde{a}^3 + 66.097\tilde{a}^4\right) \quad (2)$$

Table 3 gives the results of the three fracture tests. The deviation of the three measurements does not exceed 3% from the mean value of 75 MPa $m^{1/2}$, which consequently provides a reliable estimate for the fracture toughness K_{Ic} of the steel. This qualifies the analyzed bar steel as a medium-high toughness steel, which entails a limited risk of brittle behavior if the bars are used for structural engineering applications.

Figure 5a shows the load-CMOD data obtained from the post-fatigue tensile fracture tests of seven notched cylindrical specimens. Accordingly, the large plastic deformation experienced by all of them before fracture is entirely incompatible with the small-scale regime necessary for the stress intensity factor K to control the crack tip stress field. Despite this, K was computed by particularizing Equations (3) and (4) for the maximum tensile load F, the specimen radius R, the optically measured maximum crack depth a (Figure 5b), and the crack width b (Figure 3a), given that the ratios $\xi = a/b$ and $\zeta = a/(2R)$ appear in the applied expression of K [26,27].

$$K = Y_A \frac{F}{\pi R^2} \sqrt{\pi a} \tag{3}$$

$$Y_A = 0.67 - 0.33\xi + 5.73\zeta - 0.29\xi^2 - 2.943\xi\zeta - 22.692\zeta^2 + 2.41\xi^2\zeta + 10.684\xi\zeta^2 + 49.34\zeta^3 - 8.82\xi^2\zeta^2 - 10.16\xi\zeta^3 - 21.43\zeta^4 \tag{4}$$

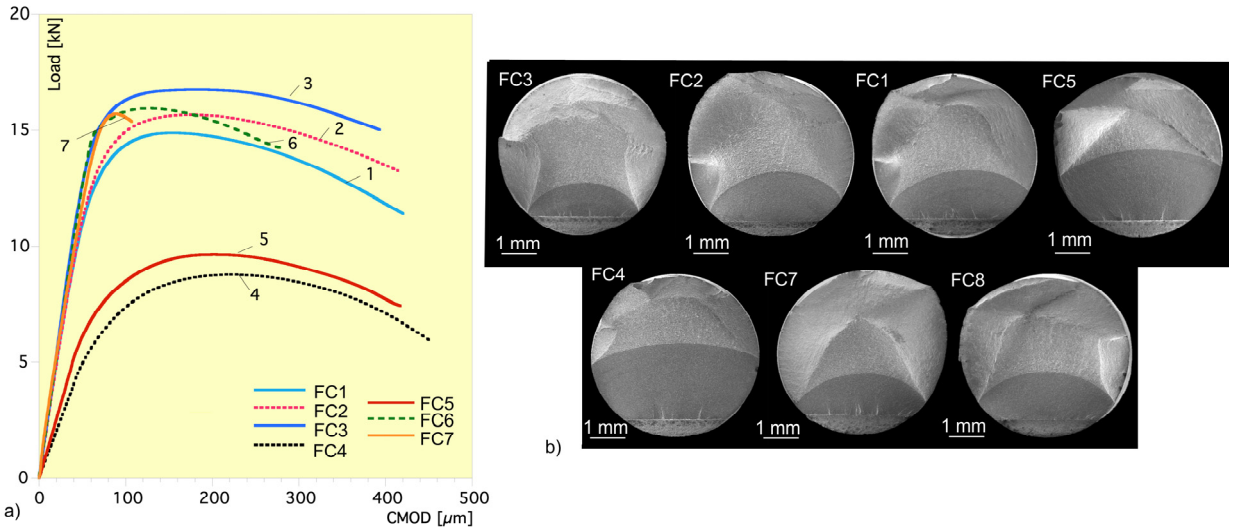

Figure 5. (**a**) Load-CMOD plots obtained from post-fatigue fracture testing of notched cylindrical specimens; (**b**) SEM images illustrating the fracture surfaces of FC1–FC7 specimens.

The crack dimensions a and c used in Equations (3) and (4) are those of the fatigue crack fronts (Figure 5b), as optically measured on the SEM images of fractured surfaces of the tested specimen.

The stress intensity factors given in Table 4 present mean and scatter values quantitatively comparable to the fracture toughness given in Table 3. The average value of the critical stress intensity factors thus computed, of 81 MPa $m^{1/2}$, is only 8% higher than the fracture toughness found from the tested short bar specimens, while the standard deviation of these seven values is 12% of the mean value. This indicates that the local condition ahead of the deepest point of the crack front is linear-elastic and controls failure, even though, as shown in Figure 5a, the global condition of specimens is elasto-plastic.

Table 4. Stress intensity factors at fracture of fatigue cracked cylindrical specimens (F_0 = 22.34 kN).

Tested Specimen	Crack Depth, a [mm]	Max. Load, F [kN]	Y_A	K_c [MPa $m^{1/2}$]
FC1	2.08	14.89	1.400	83.64
FC	1.9	15.67	1.260	76.96
FC3	1.55	16.93	1.100	66.3
FC4	2.86	8.77	2.160	86.08
FC5	2.64	9.63	2.170	97.73
FC6	1.87	16.05	1.180	73.66
FC7	1.94	15.76	1.310	81.93
				Average: 81 MPa $m^{1/2}$

3.2. Fatigue Resistance

Figure 6a shows the elliptical crack fronts developed on the fracture surfaces of FC1–FC5 specimens under the action of the different steps of cyclic loading to which they were subjected. The heat tinting at 250 °C applied for 15 min at the end of each fatigue step allowed identification and measurement of each front on the fractured surface of all five analyzed specimens. The results are given in Figure 6b and illustrate the dependence of the crack depth, expressed as a fraction a/2R of the specimen diameter, on the number of fatigue cycles. The plots indicate the tendency of the crack to initiate and grow when more than 10,000 loading cycles are exceeded. In addition, the correlation between the crack depth a and the cracked area A_f is shown in dimensionless terms in Figure 7a, expressed as respective fractions a/R and A_f/A_0 of the specimen radius R and the uncracked area A_0. These results allow the mean crack growth rate da/ΔN and the mean stress intensity factor range ΔK at the deepest point of the crack front to be computed for each fatigue step and then matched in a logarithmic plot to determine whether they obey the Paris-Erdogan Law:

$$\frac{da}{dN} = C(\Delta K)^m \tag{5}$$

given that in this equation ΔK and da/dN are, respectively, the applied stress intensity range at each fatigue cycle and the crack growth per fatigue cycle.

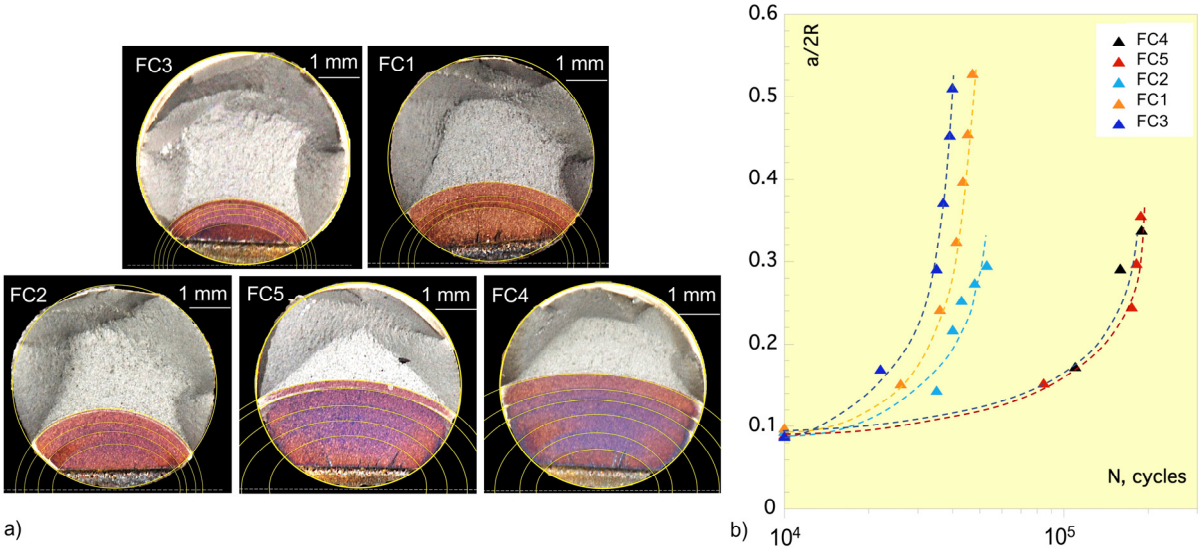

Figure 6. (**a**) Macroscopic images showing the fracture surfaces of the fatigue-tested notched cylindrical specimens with marked fatigue loading steps; (**b**) Relative crack depth a/2R as a function of specimen diameter vs. number of fatigue cycles, N.

According to the stress intensity factor K given by Equations (3) and (4) for the tested crack configuration, ΔK becomes:

$$K = Y_A\left(\frac{a}{b}, \frac{a}{2R}\right)\frac{\Delta F}{\pi R^2}\sqrt{\pi a} \tag{6}$$

where R is the specimen radius and a and c are the semi-axes of the crack front for the applied load range, ΔF. Then, Equation (5) was particularized for the load range applied during each loading step and for the mean values of the elliptic crack semi-axes measured at the initial and final crack fronts of the step. The resulting pairs of values (ΔK, da/dN) are plotted as blue dots in Figure 5b and confirm that the fatigue cracking of the tested steel follows the Paris-Erdogan Law with constants: m = 3 and C = 4.45 · 10^{-12} $MPa^{-3}m^{-1/2}$/cycle. The values of these constants reflect a typical fatigue resistance of ferrite-pearlite structural steels, significantly higher than that of martensitic steels [28].

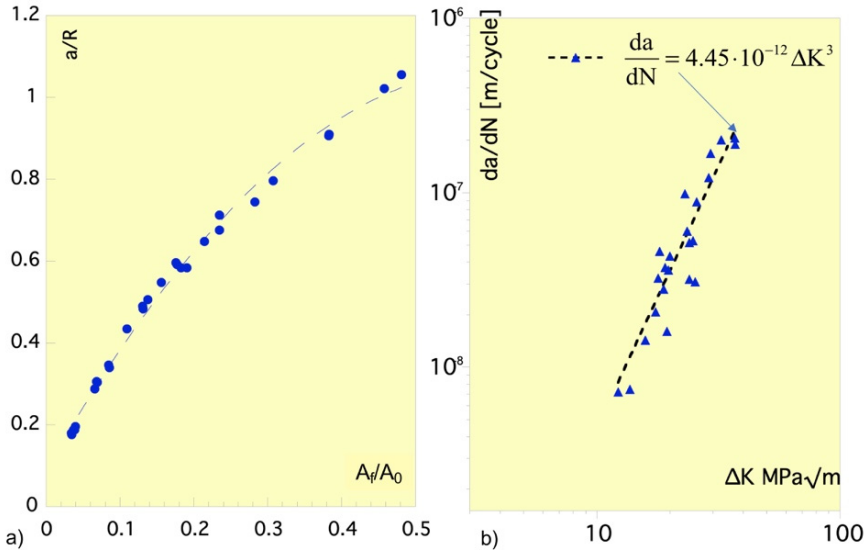

Figure 7. (**a**) Relative crack depth a/R as a function of specimen radius vs. relative fatigue cracked area A_f/A_0 as a function of uncracked area; (**b**) The Paris-Erdogan law obtained from the experimental data of FC1–FC5 tests.

3.3. Damage Tolerance of the Bar Steel

Two Failures Assessment Diagrams (FADs) given in Figure 8a,b are used to analyze the results of the previous fracture tests of the fatigue-cracked cylindrical specimens.

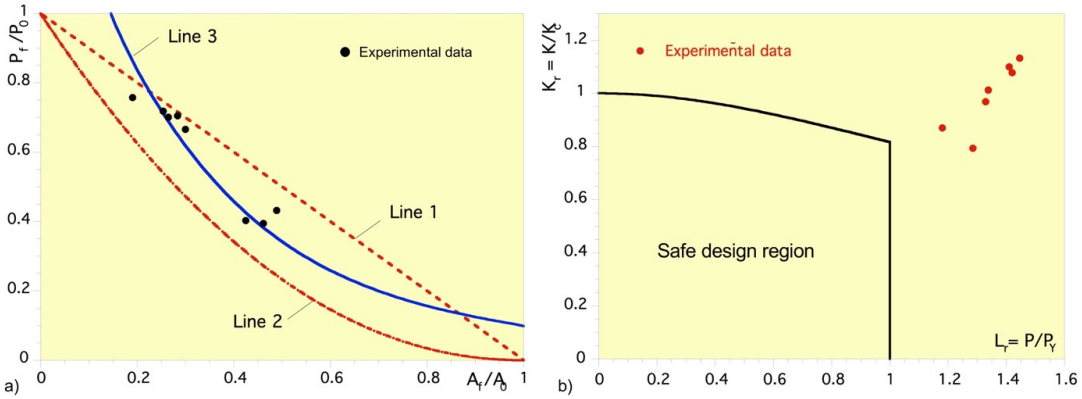

Figure 8. Failure assessment diagrams, with experimental data, involving: (**a**) damage level; (**b**) toughness and yielding capacity effects.

In Figure 8a, the experimental fracture data, namely the failure loads P_{max}, are plotted vs. the cracked areas A_f using as respective units the bearing load capacity P_0 and the cross section A_0 of specimens in undamaged condition. In addition, the diagram contains the theoretical failure predictions for plastic collapse P_Y and brittle fracture P_F. The plastic collapse occurs with the resistant ligament subjected to either pure tensile load (Line 1) or combined tension and bending load (Line 2) and depends on the compliance of the specimen to deflect transversely and align the ligament centroid with the load line. In both cases, the measured tensile strength of the bar steel is assumed to be the ideal yield strength that determines the plastic collapse. Consequently, Line 1 is given by:

$$\frac{P_Y}{P_0} = 1 - \frac{A_f}{A_0} \tag{7}$$

while, according to [29], if the aspect ratio of the crack front given by the quotient a/c belongs to the interval [0, 1], with 0 defining the straight crack front and 1 the circular crack front, Line 2 can be approximated by:

$$\frac{P_Y}{P_0} = \left(1 - \frac{A_f}{A_0}\right)^{2.1} \quad (8)$$

Then, assuming that the stress intensity factor K in the linear elastic regime controls the brittle fracture resulting from the stress and strain concentration at the crack tip, K can be used for design purposes, as loading action vs. fracture toughness K_c as a material resistance indicator. The load P_F that would cause the brittle fracture of the bar steel can be predicted from Equations (3) and (4), by particularizing the stress intensity factor K for the value of 75 MPa $m^{1/2}$ measured as fracture toughness K_c in the tests performed with pre-cracked chevron notched specimens. This prediction would generally result in an area, if plotted in the diagram shown in Figure 8a, rather than in a single curve, because two independent variables determine the crack geometry. However, given that the crack aspect ratios measured on the fracture surfaces of cylindrical specimens hardly deviate from the mean value of 1.26, a single curve, corresponding to this mean value, has been plotted as Line 3 in Figure 8a.

The positions occupied by the experimental failure data in the diagram given in Figure 8a, when compared with Line 1, Line 2, and Line 3, indicate that no failure preceding plastic collapse and caused by toughness occurs, even though they fit around Line 3. This is due to the resistant ligament of the specimens that progressively displaces towards the load line. The transversal compliance provided by the crack produces high enough stresses to surpass the tensile-bending collapse load, theoretically predicted by Equation (8), but capable of approaching the pure tensile collapse, given by Equation (7). However, toughness-controlled failure (Line 3) prevents this from being reached, so that pure tensile plastic collapse does not occur.

The failure assessment diagram adopted by Eurocode 3 for the design of steel structures against brittle failure [1] has also been used to assess the damage tolerance of the bar steel resulting from the tested cylindrical specimens. This involved computing for each specimen the stress intensity factor at fracture and the plastic collapse load by means of Equations (7) and (8). Then, the experimental failure stress intensity factor and the failure load of the specimens were plotted in the diagram given in Figure 6b after being expressed as fractions of K_r and L_r of fracture toughness (K_c = 75 M $Pam^{1/2}$) and plastic collapse load, respectively. The safe criterion of Eurocode 3 is that the design actions determine points in the diagram inside the area bounded by the ordinate with abscissa 1 and the curve given by the equation:

$$K_r = \frac{1}{\sqrt{1 + 0.5L_r^2}} \quad (9)$$

For structural members and components that obey this safety criterion, the points corresponding to failure actions instead of design actions must satisfy the opposite condition when brought into the diagram, that is, occupy positions outside the safety zone; otherwise, the design actions would be at the same time failure actions, and the safety criterion would not be met. As shown in Figure 8b, this is the case of data corresponding to the cracked cylindrical specimens when tested up to fracture. All these experimental data points are grouped in an area outside the safety zone, close to its vertex, indicating that the steel fails well beyond the limit jointly determined by fracture toughness and yielding capacity. In fact, all specimen failures occur for loads approaching the tensile bearing capacity of the resistant ligament and indicate that the steel cannot be expected to fail in a brittle manner even in damaged condition.

3.4. Fracture Micro-Mechanisms of the Bar Steel

The SEM images illustrating the fracture features of the FC2 specimen are provided in Figure 9. The red dashed line indicates the longitudinal cut (Figure 9a) that allowed the analysis of fatigue cracking and final fracture morphologies. As can be seen in Figure 9b, at the macroscopic level, the almost straight fatigue crack path is followed by a slightly inclined zigzag fracture. These crack paths are, respectively, influenced by the microstructure of fine lath martensite obtained by microalloying a medium carbon steel due to inhibited growth of prior austenite grains and by the respective types and sizes of inclusions thus generated.

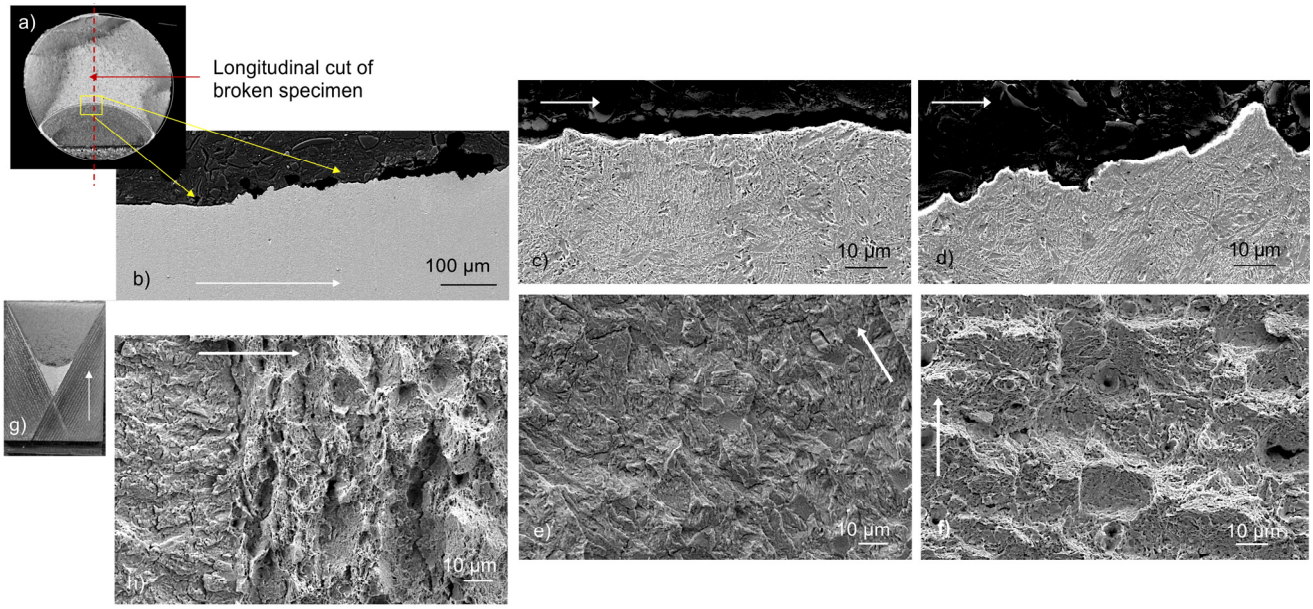

Figure 9. SEM images illustrating the cracking features of the FC2 specimen: (**a**) macroscopic image of the fracture surface; (**b**) detail of the longitudinal section capturing the fatigue and fracture crack paths; higher magnification details of the cracking paths during (**c**) fatigue and (**d**) fracture; surface topography of: (**e**) fatigue and (**f**) fracture; (**g**) macroscopic image of the SBS_2 specimen, and (**h**) higher magnification detail showing the failure initiation at the end of fatigue cracking (white arrows indicate the cracking direction).

Figure 9c shows a higher magnification detail of the little tortuous, fatigue cracking path, together with the microstructure lying below. Thus, it can be observed that the deviation of the fatigue crack path from a straight line is small because the predominant propagation takes place through the boundaries of the martensitic blocks. Nevertheless, some higher angles induced by the change in the crack path direction can also be seen in Figure 9c. These occur at the boundaries of martensitic packets or in the proximity of spherical inclusions, which behave as cracking barriers. This behavior is consistent with the SEM image of the fatigue surface shown in Figure 9e, which illustrates a complex topography consisting of quasi-cleavage facets, secondary cracks at blocks or packets boundaries, and small dimples around inclusions. The images in Figure 10a,b closely capture a small spherical inclusion of Al_2O_3, of less than 1.5 mm diameter, found on the fatigue path. The little developed dimple around it indicates a relatively weak contribution to the fatigue-generated damage into the bar steel matrix.

Figure 9d provides a detail of the resistant ligament of the FC2 specimen fractured in tension after interrupting the fatigue testing. The zigzag fracture path shown is due to both rupture and decohesion of martensite packets. The fracture surface given in Figure 9f adds new insights related to the morphology of quasi-ductile appearance, with fine dimples on dis-bonded or ruptured packets of martensite and larger voids generated around inclusions of spherical or prismatic shapes (Figure 10c,e). According to the corresponding EDX maps shown in Figure 10d,f, these are sulfide (MnS) and nitride (TiN) inclusions with sizes

comparable to those of the aluminum oxide (Al_2O_3) detected on the fatigue crack path. Therefore, despite the weak contribution of these inclusions to fatigue damage, they could influence the tensile fracture of the bar steel.

Figure 9g illustrates the fracture surface obtained after the toughness test of the SBS_2 specimen, showing how cracking initiates in the front of the convex-shaped fatigue crack. According to the higher magnification image presented in Figure 9h, the cracking front consists of a succession of transverse secondary cracks despite its quasi-ductile appearance. Interspersed among them, it can be seen that stretched and broken martensite packets and larger, deformed voids are generated around steel inclusions. Together, these morphological features explain the formation of the load pop-ins in the fracture toughness test (Figure 4b,c).

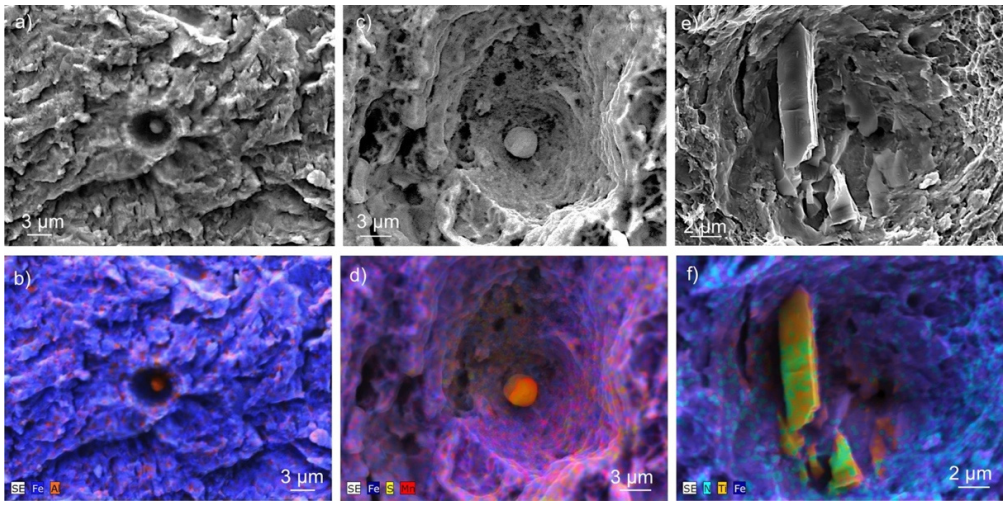

Figure 10. SEM details and EDX maps of the FC2 specimen showing the morphology of: (**a**,**b**) the fatigue crack path with an Al_2O_3 inclusion; (**c**,**d**) the fracture crack path with a MnS inclusion; (**e**,**f**) the fracture crack path with a TiN inclusion.

4. Conclusions

The experimental results of this research show that the studied ultrahigh-strength lath martensite bars produced for structural purposes are endowed with a moderately high toughness of approximately 75 MPa $m^{1/2}$, obey the Paris-Erdogan Law with the exponent m = 3, and, as most structural steels, combine in the due proportion high enough toughness and ductility to be able to avoid brittle, premature failure even in case of significant stress concentrators.

The damage tolerance analysis carried out from tensile testing of pre-cracked cylindrical specimens shows that the combination of ductility and toughness of the bar steel prevents premature tensile failures even in the presence of severe damage. The analysis was based on the joint use of two failure assessment diagrams, which allow for the separation of toughness and ductility effects on the bearing capacity of the tested cracked configurations.

The damage micro-mechanisms are consistent with the mechanical behavior and the microstructure of the bar steel. Despite the weak contribution of steel inclusions to fatigue resistance, they are determinant for pop-in formation and consequently for fracture toughness, as shown by SBS testing.

Author Contributions: Conceptualization, M.I. and A.V.; methodology, P.S. and E.S.; validation, M.I. and P.S.; formal analysis, P.S.; investigation, P.S., M.I., A.V., and E.S.; resources, M.I. and A.V.; writing—original draft preparation, M.I. and P.S.; writing—review and editing, M.I. and A.V. All authors have read and agreed to the published version of the manuscript.

Funding: The authors are gratefully acknowledging the RTI-2018-097221-B-I00 grant funded by MCIN/AEI/10.13039/501100011033 and the "ERDF A Way of Making Europe", as well as the PRE-2019-088263 grant funded by MCIN/AEI/10.13039/501100011033 and the "ESF Investing in Your Future".

Institutional Review Board Statement: Not applicable.

Informed Consent Statement: Not applicable.

Data Availability Statement: The data presented in this study are available on request from the corresponding author. The data are not publicly available due to privacy and ethical.

Conflicts of Interest: The authors declare no conflicts of interest. The funders had no role in the design of the study, in the collection, analyses, or interpretation of data, in the writing of the manuscript, or in the decision to publish the results.

References

1. *EN 1993-1-10*; Eurocode 3: Design of Steel Structures—Part 1–10: Material Toughness and Through-Thickness Properties. CEN: Brussels, Belgium, 2005.
2. *EN 1993-1-9*; Eurocode 3: Design of Steel Structures—Part 1–9: Fatigue. CEN: Brussels, Belgium, 2005.
3. ACI Committee 222. *ACI 222.2R-14 Report on Corrosion of Prestressing Steels*; American Concrete Institute: Farmington Hills, MI, USA, 2014.
4. Abela, M.C.; Landis, E. Estimating the remaining service life of in-situ grouted post-tension anchors using flaw tolerance limit plots. *Eng. Fail. Anal.* **2024**, *162*, 108349. [CrossRef]
5. Valiente, A.; Pérez-Guerrero, M.; Iordachescu, M. New testing method for assessing the cracking sensibility of stressed tendon rods in aggressive environments. *Eng. Fail. Anal.* **2016**, *68*, 244–253. [CrossRef]
6. Okada, K.; Shibata, A.; Takeda, Y.; Tsuji, N. Crystallographic analysis of fatigue fracture initiation in 8Ni-0.1C martensitic steel. *Int. J. Fatigue* **2021**, *143*, 105921. [CrossRef]
7. *ASTM A722-15*; Standard Specification for High-Strength Bars for Prestressing Concrete. ASTM International: West Conshohocken, PA, USA, 2015.
8. *prEN 10138-4*; Prestressing Steels—Part 4: Bars. CEN: Brussels, Belgium, 2005.
9. Morris, J.W. On the Ductile-Brittle Transition in Lath Martensitic Steel. *ISIJ Int.* **2011**, *51*, 1569–1575. [CrossRef]
10. Morris, J.W.; Kinney, C.; Pytlewski, K.; Adachi, Y. Microstructure and cleavage in lath martensitic steels. *Sci. Technol. Adv. Mater.* **2013**, *14*, 014208. [CrossRef]
11. Wang, C.; Wang, M.; Shi, J.; Hui, W.; Dong, H. Effect of microstructural refinement on the toughness of low carbon martensitic steel. *Scr. Mater.* **2008**, *58*, 492–495. [CrossRef]
12. Liang, Y.; Long, S.; Xu, P.; Lu, Y.; Jiang, Y.; Liang, Y.; Yang, M. The important role of martensite laths to fracture toughness for the ductile fracture controlled by the strain in EA4T axle steel. *Mater. Sci. Eng. A* **2017**, *695*, 154–164. [CrossRef]
13. Li, Y.J.; Choi, P.; Goto, S.; Borchers, C.; Raabe, D.; Kirchheim, R. Evolution of strength and microstructure during annealing of heavily cold-drawn 6.3 GP hypereutectoide pearlitic steel wire. *Acta Mater.* **2012**, *60*, 4005–4016. [CrossRef]
14. Deng, Y.; Liang, Y.; Zhao, F.; Xu, F.; Yang, M.; Long, S. Influence of Microstructure on Tensile Properties and Fatigue Crack Propagation Behavior for Lath Martensitic Steel. *Crystals* **2023**, *13*, 1392. [CrossRef]
15. Li, S.; Zhu, G.; Kang, Y. Effect of substructure on mechanical properties and fracture behavior of lath martensite in 0.1C–1.1Si–1.7Mn steel. *J. Alloys Compd.* **2016**, *675*, 104–115. [CrossRef]
16. Shin, S.E.; Nambu, S.; Kim, H.; Inoue, J.; Koseki, T.; Lee, S.J. Evaluation of factors influencing the lath martensitic deformation behavior of multi-layered steels. *Mater. Sci. Eng. A* **2020**, *785*, 139353. [CrossRef]
17. Zhang, Y.; Wang, S.; Xu, G.T.; Wang, G.; Zhao, M.H. Effect of Microstructure on Fatigue-Crack Propagation of 18CrNiMo7-6 High-Strength Steel. *Int. J. Fatigue* **2022**, *163*, 107027. [CrossRef]
18. Iordachescu, M.; Valiente, A.; Pérez-Guerrero, M.; Elices, M. Environment-assisted failure of structural tendons for construction and building applications. *Constr. Build. Mater.* **2018**, *159*, 499–507. [CrossRef]
19. Bui, T.P.; Miyashita, Y.; Mutoh, Y.; Morikage, Y.; Tagawa, T.; Handa, T.; Otsuka, Y. Fatigue crack deflection and branching behavior of low carbon steel under mechanically large grain condition. *Int. J. Fatigue* **2021**, *148*, 106217. [CrossRef]
20. Zhou, T.; Yu, H.; Wang, S. Effect of microstructural types on toughness and microstructural optimization of ultra-heavy steel plate: EBSD analysis and microscopic fracture mechanism. *Mater. Sci. Eng. A* **2016**, *658*, 150–158. [CrossRef]
21. Liu, H.-Q.; Wang, C.-M.; Zhang, H.; Huang, Z.-Y.; Wang, Q.-Y.; Chen, Q. Effects of metallic microstructures on fatigue fracture of Q345 steel. *J. Iron Steel Res. Int.* **2020**, *27*, 702–709. [CrossRef]
22. Carter, S.T.; Rotella, J.; Agyei, R.F.; Xiao, X.; Sangid, M.D. Measuring fatigue crack deflections via cracking of constituent particles in AA7050 via in situ X-ray synchrotron-based micro-tomography. *Int. J. Fatigue* **2018**, *116*, 490–504. [CrossRef]
23. *ISO 15630-3:2019*; Steel for the Reinforcement and Prestressing of Concrete. Test Methods. Part 3: Prestressing Steel. International Organization for Standardization: Geneva, Switzerland, 2019.

24. *ASTM E1304*; Standard Test Method for Plane-Strain (Chevron-Notch) Fracture Toughness of Metallic Materials. ASTM International: West Conshohocken, PA, USA, 2001.
25. Bubsey, R.; Munz, D.; Pierce, W.; Shannon, J. Compliance calibration of the short rod chevron-notch specimen for fracture toughness testing of brittle materials. *Int. J. Fract.* **1982**, *18*, 125–133. [CrossRef]
26. Shih, Y.-S.; Chen, J.-J. The stress intensity factor study of an elliptical cracked shaft. *Nucl. Eng. Des.* **2002**, *214*, 137–145. [CrossRef]
27. Toribio, J.; Álvarez, N.; González, B.; Matos, J.C. A critical review of stress intensity factor solutions for surface cracks in round bars subjected to tension loading. *Eng. Fail. Anal.* **2009**, *16*, 794–809. [CrossRef]
28. Barsom, J.M.; Rolfe, S.T. *Fatigue and Fracture Control in Structures: Application of Fracture Mechanics*, 3rd ed.; ASTM: West Conshohocken, PA, USA, 1999.
29. De Abreu, M.; Iordachescu, M.; Valiente, A. Effects of hydrogen assisted stress corrosion on damage tolerance of a high-strength duplex stainless steel wire for prestressing concrete. *Constr. Build. Mater.* **2014**, *66*, 38–44. [CrossRef]